# Magnetic resonance-guided near-infrared tomography of the breast

Ben Brooksby, Shudong Jiang, Hamid Dehghani, Brian W. Pogue, and Keith D. Paulsen
*Thayer School of Engineering, Dartmouth College, Hanover, New Hampshire 03755*

Christine Kogel, Marvin Doyley, John B. Weaver, and Steven P. Poplack
*Department of Diagnostic Radiology, Dartmouth Medical School, Hanover, New Hampshire 03755*

(Received 13 May 2004; accepted 14 September 2004; published 15 November 2004)

The design and implementation of a multispectral, frequency-domain near infrared tomography system is outlined, which operates in a MRI magnet for utilization of MR-guided image reconstruction of tissue optical properties. Using long silica optical fiber bundles, measurements of light transmission through up to 12 cm of female breast tissue can be acquired simultaneously with MRI scans. The NIR system utilizes six optical wavelengths from 660 to 850 nm using intensity modulated diode lasers nominally working at 100 MHz. Photomultiplier tube detector gain levels are electronically controlled on a time scale of 200 ms, thereby allowing rapid switching of the source to locations around the tissue. There are no moving parts in the detection channels and for each source position, 15 PMTs operating in parallel allow sensitivity down to 0.5 $pW/cm^2$ at the tissue surface. Images of breast tissue optical absorption and reduced scattering coefficients are obtained using a Newton-type reconstruction algorithm to solve for an optimal solution using the measurement data. In medical imaging, it is beneficial to compare the same tissue volume as seen by a variety of modalities, and perhaps more importantly, there is the hypothesis that one imaging system which has high spatial resolution can be used to enhance the reconstruction of another system which has good contrast resolution. In this study we explore the synergistic benefits of a combined NIR-MRI data set, specifically the ways in which MRI (i.e., high spatial resolution) enhances NIR (i.e., high contrast resolution) image reconstruction. The design, calibration, and performance of the imaging system are described in the context of preliminary phantom tests and initial *in vivo* patient imaging. Co-registered MRI validates and improves optical property estimation in 2D tomographic image reconstructions when specialized algorithms are used. © *2004 American Institute of Physics.* [DOI: 10.1063/1.1819634]

## I. INTRODUCTION

Diffuse optical tomography (DOT) with near infrared (NIR) light can be used to produce spatially resolved images of tissue optical properties. These optical property maps can be acquired at different wavelengths and combined to reveal hemoglobin concentration, oxygen saturation, water and fat content, as well as a description of scattering structures.[1–5] These latter parameters are important indicators of metabolic activity, functional processes, or presence and staging of disease. NIR diffuse tomography generally suffers from comparatively low spatial resolution due to the multiple scattering events that occur along each photon path.[6–8] However, the promise of this imaging modality lies in the fact that it affords new physical bases for contrast in tissue. For example, hemoglobin-based contrast in tumors relative to normal tissue is exceptionally high (i.e, between 100%–300%).[9] However, improving the limitations associated with its low spatial resolution is fundamental to implementing this technology clinically. *A priori* knowledge of tissue structure can be used to constrain/guide the iterative NIR image reconstruction process, and improve the spatial resolution and quantitative accuracy of recovered physiological parameters. Consequently, NIR techniques have been combined with several high spatial-resolution, structure-bearing imaging modalities including x-ray tomosynthesis,[10] ultrasound (US),[11] and magnetic resonance imaging (MRI),[12–14] to study human tissues and small animals. In this report, we present a combined NIR-MRI system for imaging female breast tissue, and explore the benefits of the combined data set in a planar tomographic geometry where the breast is imaged pendent in a standard MR breast coil.

In recent years, several important technological factors have contributed to the advancement of NIR spectral imaging applied to breast cancer characterization, including an increased understanding of light and tissue interaction, and new software-based developments in image-reconstruction algorithms for DOT.[5] NIR radiation (700–900 nm) is nonionizing, light delivery and detection instrumentation is relatively inexpensive, and uncomfortable tissue compression is not required (as in mammographic level compression). Detection systems with high signal-to-noise ratios can routinely measure NIR light transmission through 10 cm of breast tissue. This distance may increase to 12 cm for breasts with fatty composition (i.e., lower radiographic density and NIR attenuation). Photon propagation within the breast is well described by diffusion theory since the probability of photon scattering is much greater than absorption. Light transmission measurements can be combined with diffusion theory to provide robust image reconstruction of tissue optical coeffi-

 

cients. We use a Newton-type algorithm to solve for the optimal solution that provides a minimum error between the measured data and predicted response from a model of the frequency-domain diffusion equation.[15] In theory, the approach allows separation of the absorption and reduced scattering coefficients ($\mu_a$ and $\mu_s'$). Frequency-domain measurements of optical flux provide both amplitude and time-based (i.e., phase shift) information—a unique data set to solve the estimation problem associated with recovering both coefficients simultaneously.

A variety of imaging methods have achieved high-spatial-resolution imaging with acceptable to excellent soft tissue contrast, including x-ray computed tomography (CT), US, and MRI. These techniques primarily provide images of tissue structure and have a limited ability to monitor parameters related to tissue function other than through the introduction of exogeneous contrast agents. Alternatively, nuclear medicine approaches are routinely used to image tissue functions, such as metabolic fluorodeoxyglucose uptake,[16] and many commercial systems exist to co-register these images with the structural data derived from CT, US, and MRI. The combination of high resolution structural imaging with lower resolution functional information is a major emphasis in contemporary medical imaging, and customized hybrid imaging systems are being developed to avoid the complications associated with tissue movement between imaging exams, which compromises the accuracy of postprocedure co-registration.

The application of NIR tomography to provide spatially-resolved functional information, such as hemoglobin levels, oxygen saturation, water, lipid and scatterer content will likely be important, yet customized imaging systems which couple to MRI, US or CT need to be developed to evaluate and exploit this potential. The pioneering work of Ntziachristos *et al.*[13] was the first to demonstrate feasibility of the hybrid NIR-MR approach for clinical breast imaging. Their approach consisted of a co-planar array of optical source/sensors detecting time-resolved illuminations when applied to the surface of the breast. Data was presented as maps of localized optical response at each detector site but was otherwise not processed into depth-resolved images of optical property distributions. Zhu *et al.*[11] have demonstrated clinical application of a combined NIR-US system. With a handheld probe, they simultaneously measure reflection of ultrasound and modulated NIR excitations at the breast tissue surface, and construct co-registered images of structure and optical absorption and hemoglobin concentration.

One of the most challenging issues in hybrid system development is the incorporation of anatomical information as prior constraints into NIR image reconstruction. This has been explored theoretically in several successful reports.[17–22] Structural information can be used to guide functional image reconstruction through knowledge of tissue composition and location by: (i) alteration of the objective functions used in image reconstruction,[10,23] (ii) reduction of the number of unknown parameters by treating regions of the same tissue type as single zones,[13,24] or (iii) introduction of special regularization schemes that can stabilize the inverse problem and emphasize image contrasts.[10,25,26] Optimizing spatial resolution more likely will depend on the application of all three techniques, while also being strongly influenced by the signal to noise ratio of the measurements, the optical contrast available, and the number of projections used. Some investigators have successfully combined different approaches with multistage image reconstruction algorithms.[20,21] However, there is still no clear consensus on how best to utilize the structural information to enhance or improve the recovery of functional NIR information.

This work describes the first system to combine multispectral frequency-domain NIR in a planar tomographic geometry with MRI for imaging breast tissue. NIR tomography has shown the ability to localize changes in functional tissue parameters *in vivo*, and MRI has the advantage of offering a particularly rich amount of anatomical information, specifically about the layered adipose and glandular tissue structure of the breast. This system is designed to combine the benefits of both modalities into the construction of a single quantitative image. In particular, since NIR tomography has significant difficulty with the recovery of properties in layered structures, the initial information from MRI can significantly improve the estimation of breast properties, including in localized regions such as tumors.

The design and operation of the NIR-MRI system elements are described in Sec. II. The NIR component is similar to an imaging system described previously,[27] which is currently being evaluated clinically, yet has the unique design feature of having no moving parts in the detection channels, allowing significant reduction in the NIR data acquisition time. In Sec. III we outline the theoretical basis, and the practical application and utilization of image reconstruction in NIR tomography. After applying several approaches to optimizing this hybrid reconstruction, an algorithm is examined that takes advantage of the composite data set. In Sec. IV we discuss system performance and present images of phantom and breast optical properties which are both high resolution and quantitatively accurate.

## II. SYSTEM DESIGN

This section describes the four elements that comprise the NIR-MRI system: (A) light delivery, (B) detector array, (C) fiberoptic patient interface, and (D) computer control and electronics. Element (C) extends from (A) and (B) into a MRI scanner for clinical studies, as shown schematically in Fig. 1. Photographs of the rack-mounted system and patient interface are presented in Fig. 2. Section (E) briefly describes phantom fabrication, and its importance in imaging system development and validation.

### A. Light delivery

The system deploys six laser diodes: 661 nm (40 mW), 752 nm (50 mW), 785 nm (50 mW), 805 nm (50 mW), 829 nm (50 mW), and 849 nm (50 mW). Each wavelength is amplitude modulated at 100 MHz by mixing a dc current source (LDX-3220, ILX Lightwave, Bozeman, MT) and an ac current from a frequency generator (IFR-2023A, IFR Systems, Wilmington, MA), through a bias T (#5545, Picosecond Pulse Labs, Boulder, CO). Each diode is held in a laser

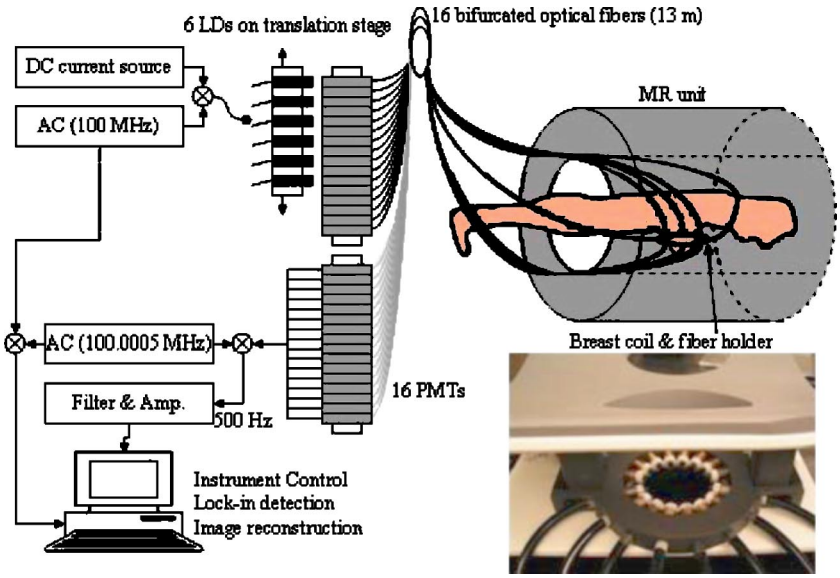


FIG. 1. (Color online) Schematic design of a dual modality NIR-MRI system (left). Frequency-domain NIR tomography is performed inside the MRI unit (upper right). Six laser diodes (660–850 nm) are amplitude modulated, and sixteen projections yield 240 measurements of amplitude and phase of transmitted light. The fiberoptic array is positioned inside the open breast coil, to allow positioning along the length of the pendant breast (bottom right).

tube (Thorlabs, Newton, NJ), and mounted on a linear translation stage (MA2515P5-S2.5 Velmex, Bloomfield, NY). This stage directs a specified wavelength into one of sixteen bifurcated optical fiber bundles which were custom designed for this application (Ceramoptec, East Longmeadow, MA). The 248-piece bundles (0.37 N.A., 0.68 packing fraction) are pure silica core (210 μm), silicone clad (230 μm) fibers suitable for transmission wavelengths from 400 nm to 2400 nm. The source light is delivered through the central seven fibers in each bundle, and the remaining fibers surrounding these are delivered to the detectors. The common end, which makes contact with the tissue, has a diameter of 4 mm. Each fiber bundle is 13 m in length and extends from the instrument cart, located outside of the MR suite, into the bore of the scanner (1.5T whole body imager, GE Medical Systems, Milwaukee, WI) to the patient interface. The efficiency of the optical switching is approximately 50%, yielding an average source power of 15 mW at the tissue surface.

### B. Light detection

For each source excitation, light transmission is recorded from 15 surface locations. This signal is measured by 15 photomultiplier tubes (PMT R6357, Hamamatsu, Japan) operating in parallel. The gain of the PMTs is varied to account for the large variation in light level between detectors depending on their distance from the source. The gains are set with PMT modules (HC120, Hamamatsu) by applying computer generated voltages between 0.4 and 1.2 V to their control lines, which sets the anode to cathode voltage between approximately 350 V to 1000 V, respectively. Using the higher gain settings, a PMT can reliably measure optical signals in the pW range. The optimal gain levels are determined prior to each imaging series. Each PMT is fixed to a particular fiber, so it is necessary to switch gains electronically during the course of data collection. A 100 MΩ resistor was used in the dynode chain of each PMT to achieve fast settling times after gain adjustment (200 ms for large gain changes). Electrical heterodyning through rf mixers (Minicircuits, Brooklyn, NY) is used to down convert the 100 MHz PMT signal to a lower frequency (500 kHz). This offset frequency is achieved with a second frequency-synthesizer which is synchronized to the one driving the laser current, and is set to 100.0005 MHz. The resulting offset frequency is filtered and amplified by a 16 channel circuit designed for

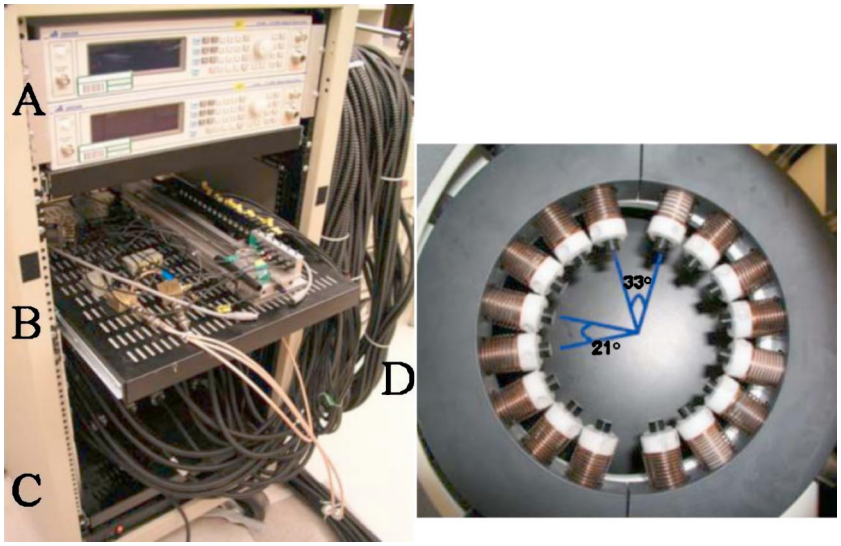


FIG. 2. (Color online) Photograph of the rack mounted, portable system (left). System components are marked, including (A) frequency generators, (B) optical switching stage, (C) PMT detection plate, and (D) optical fibers and patient interface. The fiber-patient interface (at right) can accommodate breasts 6–12 cm in diameter. A close up of the tissue coupling system shows that the fibers are spring-loaded and make light contact with the full circumference of a pendant breast.

this application (Audon Electronics, Nottingham, UK), then read by the computer. Lock-in detection is executed in software to extract amplitude and phase data for each of the detectors in parallel.

### C. Fiberoptic patient interface

The MR exam is performed using a breast array coil (MRI Devices, Waukesha, WI) that offers high-resolution imaging. The coil also provides an open architecture, which allows for the integration of the NIR-breast interface shown in Fig. 1. A circular ring machined from polyvinyl chloride (PVC) positions the common ends of the sixteen fibers around the full circumference of the pendant breast. Phosphor bronze compression springs ($k=0.09$ lbs/in., Ace Wire Spring and Form, McKees Rocks, PA) guide each fiber through holes in the ring, into light contact with the tissue surface. The ring separates into equal halves so that it can easily be moved from one breast to the other. The angular separation between each fiber is 21°, except between fibers adjacent to the line of ring devision, where the separation is 33°. The ring can be positioned vertically, such that the plane of measurements intersects the region of interest in tissue. This design allows each fiber to move independently, therefore their radial positions may vary by several millimeters. In order to avoid serious artifacts in reconstructed images, the position of each fiber must be accurately known during data acquisition. Annular fiducial markers (MM 3005, IZI Medical Products, Baltimore, MD) are fixed to each fiber and can be located with submillimeter accuracy in the MRI.

### D. Computer system

A PC running Labview software (National Instruments, Austin, TX) is used to control all light delivery and detection equipment. The laser current source and frequency generator parameters are set by a general purpose interface bus (GPIB, NI). The linear translation stage is addressed through the serial port. An analog output board (NI) is used for PMT gain control. A multipurpose data acquisition (DAQ) board acquires the 16 analog input channels and the single reference channel. This board also provides six digital output lines to the high power radio-frequency switch for the laser sources. For each source position, 15 signals from the detector system are amplified by a gain of 1000 and low pass filtered to prevent aliasing prior to the DAQ board using a 16 channel amplifier and filter network mounted in a BNC coupled box (Audon Electronics, Nottingham, UK). Data are acquired for 500 ms, and phase and amplitude of each signal are calculated and written to file. Including the time required to determine optimal gain values, measurement with 6 wavelengths takes approximately 4 min. The MR exam is controlled separately, operated in parallel, and a full volume breast MRI is of similar duration. A FORTRAN, or MATLAB based reconstruction program reads and processes the NIR data.[28–30] MR images are processed off-line with an addition to the MATLAB software package, and incorporated into a modified iterative optical property reconstruction (see Sec. III).

### E. Phantom design

Tissue-simulating phantoms with known property distributions, geometries, and imaging orientations are commonly used to validate imaging systems. We have developed a recipe for producing gelatin materials with desired optical properties, and a shelf life of several months.[31] A heated mixture of water, gelatin (G2625, Sigma Inc.), India ink (for absorption), and titanium dioxide powder (for scatter) ($TiO_2$, Sigma Inc.) is poured into a mold of a desired shape, and solidified by cooling to room temperature. Variation in the water concentration provides MR contrast, and variable gel stiffness. The phantom imaged here (Sec. IV B) combines three gels with different optical properties in an irregular structure.

## III. DATA PROCESSING AND IMAGE RECONSTRUCTION

Quantitative NIR imaging with model-based methods requires (A) important instrument calibration procedures, and (B) a reconstruction algorithm that incorporates an accurate model of light propagation in tissue.

### A. System calibration

Calibration issues and other practical considerations associated with our NIR imaging approach have been discussed in detail elsewhere.[29] Two important procedures are briefly noted here: (1) detector calibration, and (2) homogeneous phantom calibration. First, the amplitude and phase response of each detection channel must be characterized in order to remove systematic noise in the data acquisition hardware. Each detector is exposed to the same optical signal, and the differences in log amplitude and phase are used as correction factors. The log amplitude response of the PMT is plotted against the log of the input power for each gain setting. A log–log regression is performed and the coefficients are used to calibrate detected PMT amplitude in terms of optical power. The phase does not fluctuate significantly with changing light level for a single gain setting (i.e., minimal phase-amplitude cross-talk), but is altered dramatically with changing gain. Relative phase differences between detectors are stored for calibration. These calibration curves are very similar to those created by McBride *et al.*[27] This characterization needs to be performed only once as long as the system is not modified.

The second important practical procedure is the correction for inter fiber variations and coupling issues, which is accomplished through a homogeneous phantom calibration process.[29,32] This accounts for offsets due to optical fiber differences in transmission and alignment, as well as any errors in discretization or data-model mismatch. A homogeneous phantom is generally measured each day, and after system changes. The differences between data measured from the phantom, and data calculated from the model are stored and subtracted from measurements of the heterogeneous phantom or tissue under investigation. A homogeneous fitting algorithm is used to determine the $\mu_a$ and $\mu_s'$ values supplied to the model calculation. This algorithm can also be used to calculate the initial optical properties specified in

iterative reconstruction of heterogeneous media. When dealing with tissues having arbitrary shape, the effectiveness of this fitting algorithm and homogeneous phantom calibration hinges on the accurate specification of source and detector locations. The ability to extract accurate fiber positions from MRI scans preserves the integrity of this method for nonuniform boundary data.

### B. FEM analysis

Data acquired from the detection system is processed by a FEM based reconstruction algorithm to generate tomographic images of absorption and reduced scattering coefficients simultaneously. The algorithm exploits the frequency-domain diffusion equation approximation to light behavior in a highly scattering medium,[28]

$$-\nabla\cdot D(\mathbf{r})\nabla\Phi(\mathbf{r},\omega)+\left(\mu_a(r)+\frac{i\omega}{c}\right)\Phi(\mathbf{r},\omega)=S(r,\omega), \tag{1}$$

where $S(r,\omega)$ is an isotropic light source at position $r$, $\Phi(r,\omega)$ is photon density at $r$, $c$ is the speed of light in tissue, $\omega$ is the frequency of light modulation, $\mu_a$ is the absorption coefficient, and $D=1/[3(\mu_a+\mu_s')]$ is the diffusion coefficient. The reduced (transport) scattering coefficient is given by $\mu_s'=\mu_s(1-g)$, where $g$ is the mean cosine of the single scatter function (the anisotropy factor), and $\mu_s$ is the scattering coefficient.

For a given $\mu_a$ and $\mu_s'$ distribution, the diffusion equation is used to predict the optical flux at the detector sites for each source excitation. In the inverse problem (image reconstruction), the goal is the estimation of optical properties at each FEM node, based on measurements of optical flux at the detector sites on the tissue surface. This is achieved numerically by minimizing the difference between the calculated data $\Phi^C$, and measured data, $\Phi^M$, for all source/detector combinations ($NM$). Typically,

$$\chi^2=\sum_{i=1}^{NM}(\Phi_i^C-\Phi_i^M)^2 \tag{2}$$

is minimized in a least squares sense by setting the first derivative equal to zero, and using a Newton–Raphson approach to find the set of optical property values which approximate the point of stationarity. We use a Levenberg Marquardt algorithm, and repeatedly solve the equation

$$a=(J^TJ+\lambda I)^{-1}J^Tb, \tag{3}$$

where $b=(\Phi^C-\Phi^M)^T$ is our data vector, and $a$ is the solution update vector, $a=\lfloor\delta D_j;\delta\mu_{aj}\rfloor$, defining the difference between the true and estimated optical properties at each reconstructed node$j$. Here, $\lambda$ is a regularization factor to stabilize matrix inversion and $J$ is the Jacobian matrix for our model, which is calculated using the Adjoint method.[33]

Improving NIR reconstructions by incorporating MRI data has been explored in previous work,[22,23] and by other authors.[13,21,24] Techniques used to produce the images shown in Sec. IV include: (i) accurately defining the imaging volume, (ii) tailoring a regularization scheme which optimizes the reconstructed contrast of a suspicious area in the image,

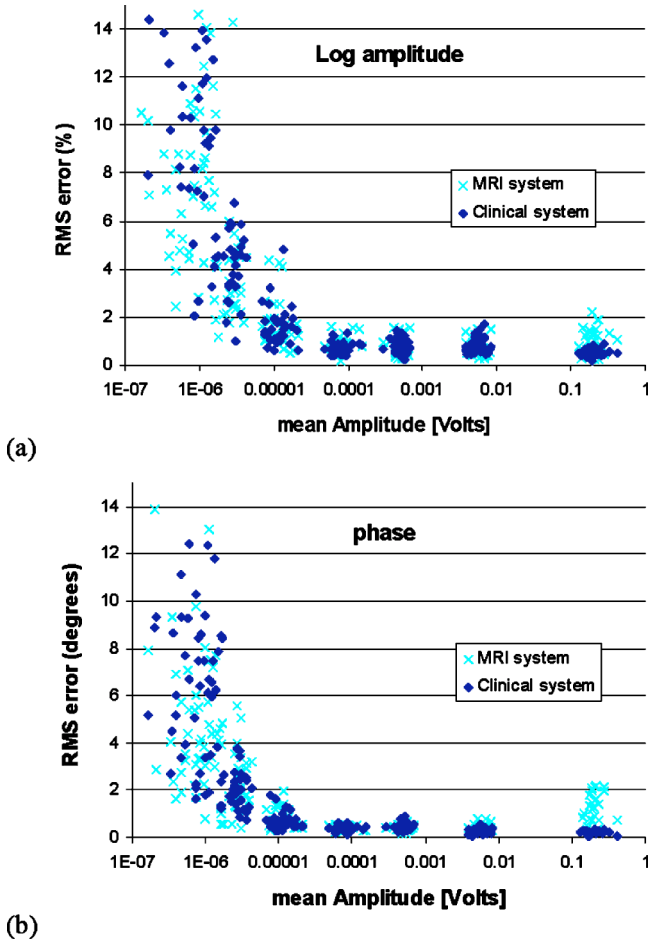


FIG. 3. (Color online) Repeatability assessment for (a) log amplitude and (b) phase of NIR component of combined NIR-MRI system and stand-alone NIR tomography system at Dartmouth. The performance of the two systems is comparable. In routine operation, PMT voltage signals are above $1.0\times10^{-5}$ V.

and (iii) reducing the number of unknown parameters by segmenting tissue types visible in the MRI. Defining the imaging volume, (i), is relatively straight forward and can be accomplished by creating a structured finite element mesh from the MRI. This mesh will often contain regional differences depending on tissue types present, and an irregular outer boundary due to impressions caused by fiber-tissue contact. In simulation studies, not presented here, it has been found that image reconstruction accuracy is easily degraded if the mesh (2D or 3D) does not represent the true outer tissue boundary. Step (ii) can be accomplished by changing $\lambda I$ in Eq. (3) to $\lambda A$, where $A$ is a regularization matrix, or filter matrix. Regularization can be thought of as a smoothing operator, where one can apply selective smoothing by linking together the property updates for all nodes associated with the same region or tissue type. Modifications to the Jacobian matrix size in a parameter reduction technique are used to implement step (iii).[23]

## IV. PERFORMANCE AND EXPERIMENTAL RESULTS

In this section we (A) compare measurements from this system to those from a similar NIR tomography instrument

TABLE I. Optical properties at 785 nm for 15 tissue simulating phantoms, and % differences from values determined using another NIR tomography system.

| | $\mu_a$(mm$^{-1}$) (NIR-MRI) | % difference | $\mu_s'$(mm$^{-1}$) (NIR-MRI) | % difference |
|---|---|---|---|---|
| Mean | 0.0055 | −6.2 | 1.34 | 9.1 |
| Max | 0.0102 | −23.4 | 1.91 | 29.6 |
| Std. Dev. | 0.0024 | 8.7 | 0.41 | 7.9 |

described previously[27] for a number of tissue simulating phantoms. NIR-MRI phantom studies are described in (B), and *in vivo* images are shown in (C). For all results presented here, we used a single laser diode (785 nm) for convenience, and 2D modeling and image reconstruction. System performance and image quality at the other five wavelengths are comparable, and 3D imaging is readily achievable.

### A. System performance

Measurement repeatability in terms of phase and log amplitude error was assessed by serially imaging a phantom with optical properties similar to those of average breast tissue ($\mu_a$=0.004, $\mu_s'$=1.35). The average rms error at each detector site was determined to be 0.26% in ac intensity and 1.04° in phase. These values compare with those obtained from the system described by McBride *et al.* (0.32% in ac intensity and 0.48° in phase).[27] rms error for each of the 240 source-detector combinations for both systems is plotted versus the PMT signal in Fig. 3. For both phase and amplitude, error sharply increases when incident light falls below approximately 0.5 pW. These points are excluded in the calculation of average rms error. As an additional comparison, we used both devices to measure a collection of homogeneous phantoms ($N$=15) of varying diameters (73–91 mm) and optical properties ($\mu_a$=0.0023–0.0102 mm$^{-1}$, $\mu_s'$=0.33–1.91 mm$^{-1}$). After processing the measurements with the calibration procedure described in Sec. III, we used the homogeneous fitting algorithm to determine a single $\mu_a$ and $\mu_s'$ for each material. Table I shows the optical coefficients obtained with the NIR-MRI system, along with a measure of their discrepancy with those obtained with our stand-alone DOT instrumentation. We observed good agreement between the two systems, consistent throughout the range of phantom properties. The absorption and scattering coefficients show correlation coefficients of $R^2$=0.984 and $R^2$=0.980, respectively.

TABLE II. Approximate optical properties of gelatin phantom.

| | Outer layer | Inner layer | Inclusion |
|---|---|---|---|
| $\mu_a$(mm$^{-1}$) | 0.0044 | 0.0062 | 0.02 |
| $\mu_s'$(mm$^{-1}$) | 0.51 | 0.68 | 0.9 |

### B. Phantom imaging

Due to the limited spatial resolution of DOT, layered media, small objects, and low contrast heterogeneity pose key challenges in image reconstruction. The capability of the presented system to address these challenges was investigated by imaging a phantom comprised of three gels with different optical properties. The phantom is cylindrical and the boundary between the outer layer and inner layer is irregular. A two centimeter spherical inclusion is embedded within the inner layer. The optical coefficients of each gel are known (Table II), as each material was created using a practiced recipe to give desired values. Furthermore, the true value of each layer was validated by creating a separate homogenous phantom for each layer (at the same time as creating layered phantom) and measuring bulk properties with a homogeneous fitting algorithm. To increase MRI contrast between layers, Omniscan™ (gadodiamide) was added to the inner layer (0.005 g/ml).

A photograph of the phantom, alongside another spherical inclusion is shown in Fig. 4(a). Figure 4(b) shows a T1-weighted, gradient echo MRI (25 ms TR, 3 ms TE, 45° flip angle) crosssection of the phantom in the plane of the optical fibers. This was used to create a 2D structured finite element mesh and to locate the positions of the 16 fibers [Fig. 4(c)]. Fiber fiducials were not used in this experiment, but the 16 impressions caused by each optical fiber are clearly visible around the perimeter of the gel. Each of the three regions are also visible, corresponding to each of the three types of optically variant gel. 3D meshing and imaging is also possible, given that a stack of MR slices represent the full volume

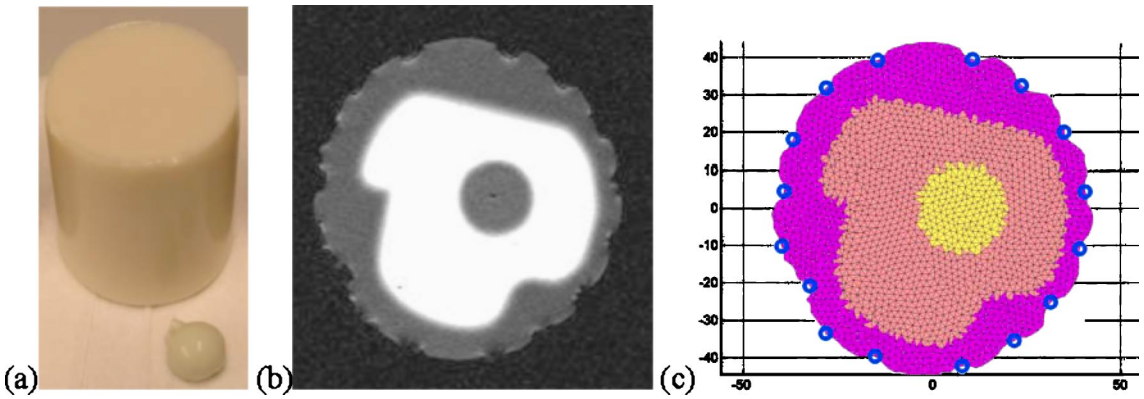


FIG. 4. (Color online) (a) The gelatin phantom. (b) T1-weighted MRI image of the structure of the phantom cross section. The inner layer (light region) contains gadodiamide for MR contrast (0.005 g/ml). The inner inclusion is a 2 cm diameter sphere. (c) Finite element mesh derived from the three-layered structure image in (b). The circles on the outer boundary indicate the fiber locations. Axes are in millimeters.

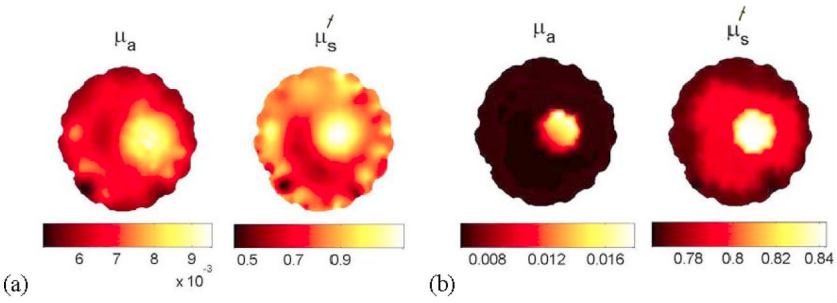


FIG. 5. (Color online) Images in (a) show absorption coefficient (left) and reduced scattering coefficient (right) reconstructions without MRI guidance. In (b), reconstructions improve when the interior structural information of the MRI is incorporated. Comparing these two images, the latter has a reduction in artifacts in the reduced scattering coefficient image, and both the spatial resolution and contrast have improved. The recovered values compare favorably with the approximate true values shown in Table II.

structure of the phantom. The system design allows for NIR data acquisition in multiple planes if desired.

Using log amplitude and phase data, images of optical properties were reconstructed with two different algorithms. The first algorithm solves Eq. (3) without *a priori* guidance, except for the use of the mesh and source locations from Fig. 4(c). The corresponding reconstructed images are presented in Fig. 5(a). The second algorithm uses the layered structure from the MRI to constrain Eq. (3). The regularization parameter associated with each reconstructed node is adjusted based upon its location and area of influence. Lower values are used for small regions close to the center of the reconstructed volume, whereas peripheral regions (which are prone to large artifacts) have larger regularization. A regularization matrix ($A$), or filter matrix, based upon the *a priori* structural information from the MRI was also used to further improve the algorithm. The optimal values for $\lambda$ and $A$ were determined in simulation studies of this geometry, using similar contrast and noise levels. These can also be chosen automatically once an empirical knowledge of their effect is established. The images reconstructed from this modified constrained algorithm are shown in Fig. 5(b).

Qualitatively, the algorithm that uses MRI information to guide the iterative process performs much better. The optical property images in Fig. 5(a) are blurry and "edge artifacts" are clearly visible, especially for $\mu_s'$. The absorbing sphere near the center of the phantom is recovered with poor spatial resolution, and its contrast is underestimated. The property maps in Fig. 5(b) have improved resolution. Spatial resolution and contrast of the spherical inclusion are better. As a quantitative measure of the accuracy of image reconstruction, we compute the rms error between the target image and the reconstructions, node by node. This measure indicates a dramatic improvement for the second method [$\mathrm{rms}(\mu_a)=0.0024$, $\mathrm{rms}(\mu_s')=0.19$] relative to the first [$\mathrm{rms}(\mu_a)=0.0034$, $\mathrm{rms}(\mu_s')=0.25$].

### C. *In vivo* imaging

The Institutional Review Board (IRB) at the Dartmouth Hitchcock Medical Center approved this clinical examination protocol, and written informed consent was obtained from all volunteering women. Figures 6(a) and 6(b) show a photograph of a subject lying on the examination platform, and an anatomical axial MR image through the breast. NIR measurements (4 wavelengths in this case) and a full volume MRI (50 coronal slices, 25 ms TR, 6 ms TE, 45° flip angle, 2 mm slice thickness) were obtained in less than 10 min. Fig. 7(a) shows an anatomically coronal MRI with 16 fiducial-marked fibers (appearing as bright white spots outside the breast). The radiographic density of this participant is heterogeneously dense (HD), and a large interior region of glandular tissue is easily defined in the FEM mesh shown in Fig. 7(b).

As with the phantom study, we present images of $\mu_a$ and $\mu_s'$ at 785 nm reconstructed with two different algorithms. The first result, obtained by solving Eq. (3), without *a priori* guidance, is shown in Fig. 7(c). As expected, we see higher absorption and scatter in the glandular region (central) relative to the adipose tissue (peripheral). However, the region of increase does not span the full area expected, and heterogeneity is visible (especially around the perimeter of the image). The second algorithm assumes homogeneous optical properties for each tissue type, and utilizes parameter reduction,[23] which leads to a "fitting" for four values: $\mu_{a\ \mathrm{adipose}}=0.003$, $\mu_{s\ \mathrm{adipose}}'=0.93$, $\mu_{a\ \mathrm{glandular}}=0.006$, $\mu_{s\ \mathrm{glandular}}'=1.12$ [Fig. 7(d)]. This algorithm is robust to noise and converges after a few iterations. The result is quantita-

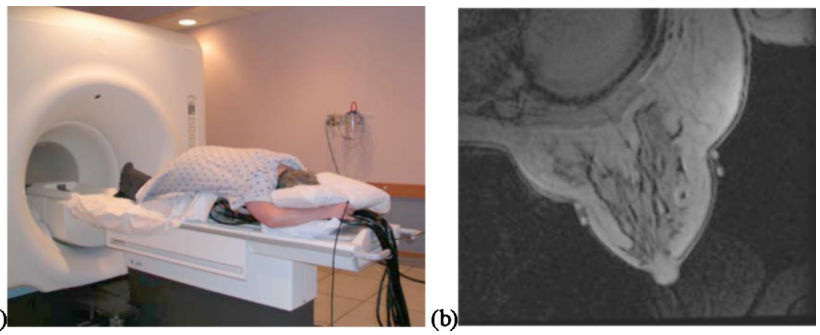


FIG. 6. (Color online) Photograph in (a) shows a female volunteer prepared for the simultaneous MRI-NIR exam. In an anatomically axial T1-weighted MRI slice from the right breast, (b), fiducial markers (outside the breast) indicate the location of the fiber plane.

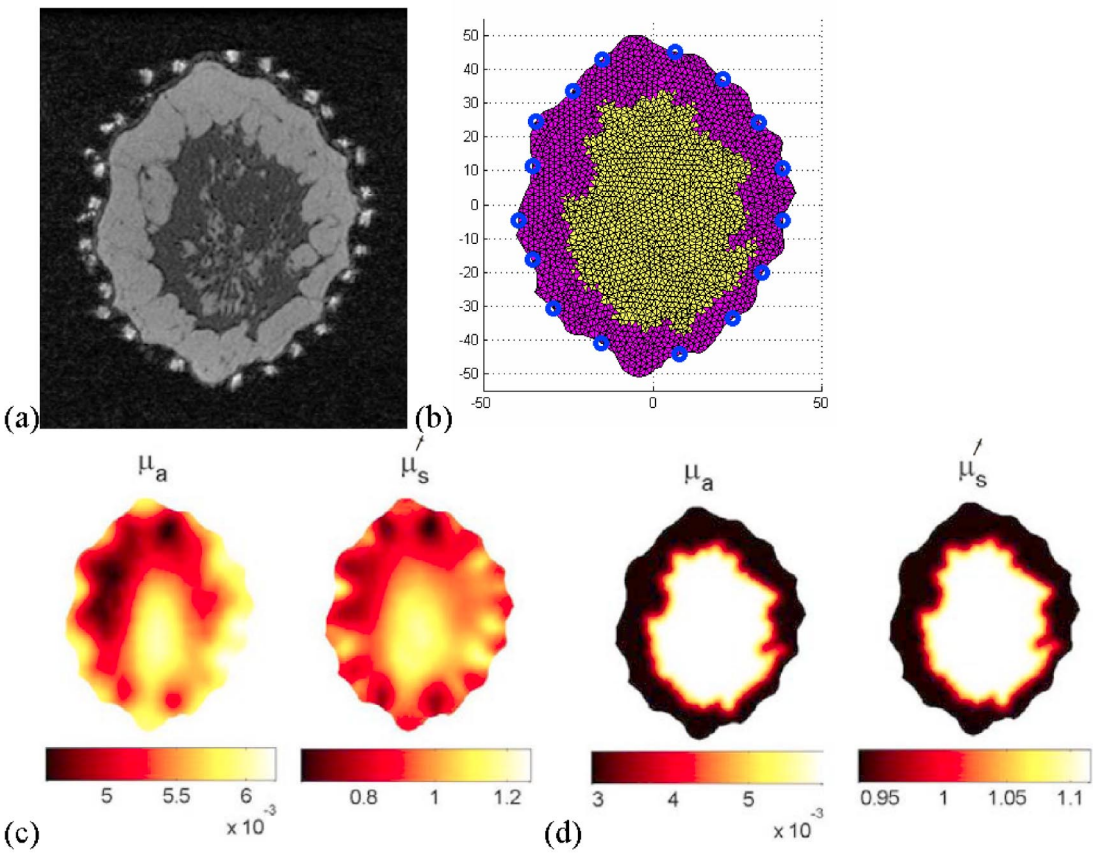


FIG. 7. (Color online) In (a), an anatomically coronal T1-weighted MRI displays adipose (outer) and glandular (inner) tissue types. A two layer structured FEM mesh and source locations, created from (a), is shown in (b). Absorption and reduced scattering coefficient ($mm^{-1}$) reconstructions in (c) are obtained without utilizing the internal structure of (b). In (d), MRI data guides a two-region parameter fitting algorithm. Relative to (c), resolution has improved and contrast has increased—showing higher absorption and scatter in glandular relative to adipose tissue.

tively logical, and similar values are recovered using spatially varying regularization (as described in the phantom reconstruction).

## V. DISCUSSION

This article describes a novel *in vivo* breast imaging system that synergistically combines NIR tomography with MRI. Tissue structures visible with high resolution in MRI can be applied *a priori* to optical property reconstructions from frequency-domain NIR measurements. Thus, the reconstruction process can be optimized to produce high resolution, quantitatively accurate maps of absorption and reduced scattering coefficients, and ultimately physiologically relevant parameters. Various physiological tissue types exhibit significant contrast in the NIR, primarily though, the combined system could be very effective at locating and diagnosing breast tumors.

The NIR component provides multispectral (6 wavelengths) frequency-domain (log amplitude and phase) data from 16 fiber-tissue contact positions around the breast's circumference. Data acquisition is fully automated, and a complete set of measurements (240 source-detector pairs) for one wavelength requires approximately 40 s. Light detection is highly sensitive (subpicowatt limit) with low noise (rms $<0.26\%$, $<1.04°$ in phase). All optical elements and controls are mounted in a portable cart, and operation inside strong magnetic fields is facilitated with long optical fibers and an easy-to-use positioning system/patient interface.

The deployment of dual modality NIR imaging systems in clinical applications has been limited to date, mainly because of the complexity of the image reconstruction problem. Here, a representative phantom and *in vivo* study using one wavelength (785 nm) are presented. We have shown that co-registered MRI validates and improves optical property estimation in 2D tomographic image reconstructions when specialized algorithms are used. Future work will involve 3D modeling and reconstruction, which could further improve both qualitative and quantitative aspects of the recovered coefficient values.

Preliminary results are encouraging, and have allowed us to optimize reconstruction techniques, and automate constraint selection. We have performed several phantom studies, and demonstrated the feasibility of imaging volunteers with healthy breasts. Through the study of more healthy subjects, with different radiographic densities, we aim to compare functional parameters of adipose versus glandular tissue. To test the system's ability at diagnosing tumors, cancer patients will be recruited, and the simultaneous exam will likely involve MR contrast enhancement.

## ACKNOWLEDGMENTS

The authors would like to express sincere gratitude to Gordon Ehret and Richard Johnson for their fine fabrication

work. This work has been sponsored by the National Cancer Institute through Grants Nos. RO1CA78734, PO1CA80139, and DAMD17-03-1-0404.

[1] V. Ntziachristos, A. H. Hielscher, A. G. Yodh, and B. Chance, IEEE Trans. Med. Imaging **20**, 470 (2001).
[2] B. W. Pogue, S. P. Poplack, T. O. McBride, W. A. Wells, O. K. S. Osterman, U. L. Osterberg, and K. D. Paulsen, Radiology **218**, 261 (2001).
[3] S. Srinivasan, B. W. Pogue, S. Jiang, H. Dehghani, C. Kogel, S. Soho, J. J. Gibson, T. D. Tosteson, S. P. Poplack, and K. D. Paulsen, Proc. Natl. Acad. Sci. U.S.A. **100**, 12349 (2003).
[4] B. J. Tromberg, N. Shah, R. Lanning, A. Cerussi, J. Espinoza, T. Pham, L. Svaasand, and J. Butler, Neoplasia **2**, 26 (2000).
[5] S. R. Arridge, Inverse Probl. **15**, R41 (1999).
[6] H. Dehghani, B. W. Pogue, S. Jiang, B. A. Brooksby, and K. D. Paulsen, Appl. Opt. **42**, 3117 (2003).
[7] V. Chernomordik, A. H. Gandjbakhche, M. Lepore, R. Esposito, and I. Delfino, J. Biomed. Opt. **6**, 441 (2001).
[8] D. A. Boas, K. Chen, D. Grebert, and M. A. Francheschini, Opt. Lett. **29**, 1506 (2004).
[9] B. W. Pogue, S. Jiang, H. Dehghani, C. Kogel, S. Soho, S. Srinivasan, X. Song, T. D. Tosteson, S. P. Poplack, and K. D. Paulsen, J. Biomed. Opt. **9**, 541 (2004).
[10] A. Li, E. L. Miller, M. E. Kilmer, T. J. Brukilaccio, T. Chaves, J. Stott, Q. Zhang, T. Wu, M. Choriton, R. H. Moore, D. B. Kopans, and D. A. Boas, Appl. Opt. **42**, 5181 (2003).
[11] Q. Zhu, N. G. Chen, and S. H. Kurtzman, Opt. Lett. **28**, 337 (2003).
[12] B. W. Pogue, H. Zhu, C. Nwaigwe, T. O. McBride, U. L. Osterberg, K. D. Paulsen, and J. F. Dunn, Oxygen Transport to Tissue, Vol. XXIV, p. 215 (2002).
[13] V. Ntziachristos, A. G. Yodh, M. D. Schnall, and B. Chance, Neoplasia **4**, 347 (2002).
[14] G. Gulsen, H. Yu, J. Wang, O. Nalcioglu, S. Merritt, F. Bevilacqua, A. J. Durkin, D. J. Cuccia, R. Lanning, and B. J. Tromberg, Technol. Cancer Res. Treat. **1**, 1 (2002).
[15] K. D. Paulsen and H. Jiang, Med. Phys. **22**, 691 (1995).
[16] M. Tatsumi, C. Cohade, Y. Nakamoto, and R. L. Wahl, Radiology **229**, 831 (2003).
[17] R. L. Barbour, H. L. Graber, J. Chang, S. S. Barbour, P. C. Koo, and R. Aronson, IEEE Comput. Sci. Eng. **2**, 63 (1995).
[18] A. H. Barnett, J. P. Culver, A. G. Sorensen, A. Dale, and D. A. Boas, Appl. Opt. **42**, 3095 (2003).
[19] V. Ntziachristos, X. H. Ma, and B. Chance, Rev. Sci. Instrum. **69**, 4221 (1998).
[20] M. Torregrossa, C. V. Zint, and P. Poulet, Opt. Tomography and Spectroscopy of Tissue V (2003).
[21] M. Schweiger and S. R. Arridge, Phys. Med. Biol. **44**, 2703 (1999).
[22] B. W. Pogue, T. O. McBride, C. Nwaigwe, U. L. Osterberg, J. F. Dunn, and K. D. Paulsen, Proc. SPIE **3597**, 484 (1999).
[23] B. A. Brooksby, H. Dehghani, B. W. Pogue, and K. D. Paulsen, IEEE J. Sel. Top. Quantum Electron. **9**, 199 (2003).
[24] N. G. Chen, P. Guo, S. Yan, D. Piao, and Q. Zhu, Appl. Opt. **40**, 6367 (2001).
[25] B. W. Pogue, T. O. McBride, J. Prewitt, U. L. Osterberg, and K. D. Paulsen, Appl. Opt. **38**, 2950 (1999).
[26] M. Belge, M. E. Kilmer, and E. L. Miller, Inverse Probl. **18**, 1161 (2002).
[27] T. O. McBride, B. W. Pogue, S. Jiang, U. L. Osterberg, and K. D. Paulsen, Rev. Sci. Instrum. **72**, 1817 (2001).
[28] H. Dehghani, B. W. Pogue, S. P. Poplack, and K. D. Paulsen, Appl. Opt. **42**, 135 (2003).
[29] T. O. McBride, B. W. Pogue, U. L. Osterberg, and K. D. Paulsen, Oxygen Transport to Tissue Vol. XXIV, p. 85 (2002).
[30] B. W. Pogue, S. Geimer, T. O. McBride, S. Jiang, U. L. Osterberg, and K. D. Paulsen, Appl. Opt. **40**, 588 (2001).
[31] D. Li, P. M. Meany, T. D. Tosteson, S. Jiang, T. Kerner, T. O. McBride, B. W. Pogue, A. Hartov, and K. D. Paulsen, Med. Phys. **30**, 2194 (2003).
[32] S. Jiang, B. W. Pogue, T. O. McBride, M. M. Doyley, S. P. Poplack, and K. D. Paulsen, J. Electron. Imaging **12**, 613 (2003).
[33] S. R. Arridge and M. Schweiger, Appl. Opt. **34**, 8026 (1995).